Journal of Power Sources 684 (2026) 240442

Contents lists available at ScienceDirect

Journal of Power Sources

journal homepage: www.elsevier.com/locate/jpowsour

Direct-ink writing printed cathodes based on different active materials for lithium-ion batteries

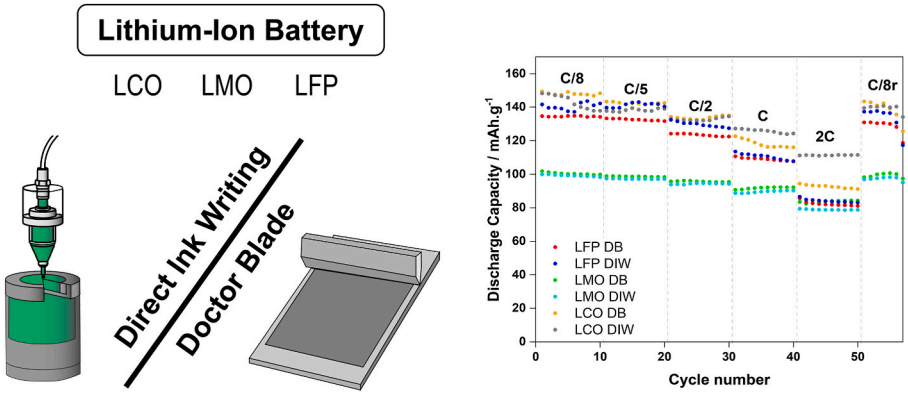
Rafael S. Pinto [a,b], Francisco Macedo [b], Maria M. Silva [a], Carlos M. Costa [b,c], Senentxu Lanceros-Mendez [b,d,e,*], Renato Gonçalves [a,**]

[a] Chemistry Centre of the University of Minho (CQ-UM), Braga, 4710-057, Portugal
[b] Physics Centre of Minho and Porto Universities (CF-UM-UP) and Laboratory of Physics for Materials and Emergent Technologies, LapMET, University of Minho, Braga, 4710-057, Portugal
[c] Institute of Science and Innovation for Bio-Sustainability (IB-S), University of Minho, Campus de Gualtar, Braga, 4710-057, Portugal
[d] BCMaterials, Basque Center for Materials, Applications and Nanostructures, UPV/EHU Science Park, Leioa, 48940, Spain
[e] IKERBASQUE, Basque Foundation for Science, Bilbao, 48009, Spain

HIGHLIGHTS

- LFP, LCO and LMO based cathodes have been obtained by DB and DIW processes;
- Higher cathode's performance is verified for DIW cathodes at higher C-rates;
- LCO DIW cathodes show a discharge capacity of 111.3 mAh g^{-1} at a rate of 2C;
- DIW cathodes show an improved or very similar battery performance, compared to DB.

GRAPHICAL ABSTRACT



ARTICLE INFO

Keywords:
Cathode
Active material
Direct ink writing
Printing
Sustainability
Electrodes

ABSTRACT

Rising demand for portable electronic leads to development of energy storage systems with improved energy-/power-density. In this work, it is proposed the use of different active materials allied to Direct-Ink Writing (DIW) printing technology for the development of lithium-ion batteries cathodes. $LiFePO_4$, $LiMn_2O_4$ and $LiCoO_2$ active materials were used to produce cathodes based on Doctor Blade (DB) and DIW processing techniques to assess the influence of active filler and preparation technique on cathode's characteristics. The results demonstrate that the DIW processing technique allows to improve cathode properties also allowing the possibility of new designs and shapes necessary for portable applications. DIW induces a smooth morphology on cathode surface, lowering the presence of cracks, for the same preparation conditions as in DB. An increase of apparent lithium-ion diffusion coefficient for $LiFePO_4$ and $LiMn_2O_4$ was observed in DIW samples, where $LiFePO_4$ increase from

* Corresponding author.
** Corresponding author.
E-mail addresses: senentxu.lanceros@bcmaterials.net (S. Lanceros-Mendez), r.goncalves@quimica.uminho.pt (R. Gonçalves).

https://doi.org/10.1016/j.jpowsour.2026.240442
Received 17 March 2026; Received in revised form 4 May 2026; Accepted 16 May 2026
Available online 22 May 2026
0378-7753/© 2026 The Authors. Published by Elsevier B.V. This is an open access article under the CC BY license (http://creativecommons.org/licenses/by/4.0/).

1.71×10^{-7} cm^2 s^{-1} (DB) to 3.70×10^{-7} cm^2 s^{-1} (DIW). Half-cells performance demonstrated an improved or very similar discharge capacities for the samples prepared by DIW, compared to DB. $LiFePO_4$ cathode discharge capacities of 134.8 mAh.g^{-1} (DB) and 137.5 mAh.g^{-1} (DIW) at C/8-rate is observed. The study demonstrates the capability of DIW technique to produce customized, flexible and high-performance cathodes.

1. Introduction

The 4th Industrial Revolution allied to Internet of Things (IOT) paradigm, has promoted the development of portable electronic devices and their number has been growing since then [1]. These devices have improved their energy-demanding features, exercising pressure on the materials used in the different lithium-ion battery (LIB) components, mainly on critical materials, such as cobalt [2].

LIBs are one of the most used types of energy storage systems and they are well established in the energy storage field, due to their long life cycling and energy and power densities [3]. These characteristics made LIB the best option for applications in all ranges of electronic devices, from the smaller ones to electric vehicles [4]. With this in mind, it is essential to further improve processing techniques and materials in order to improve integration into devices, optimize performance and reduce the pressure exerted on natural reserves [5–7]. Recent advances in a new generation of batteries based on novel materials such as carbon materials, silicon hollow spheres and nanofiber active materials, associated to improved production techniques, such as additive manufacturing techniques, are reviewed in Ref. [8]. In this context, different materials have been used for electrode development, taking into account the specific application requirements, such as high power or energy density.

The LIB capacity is determined by the electrodes, as they release and store the lithium-ions in their structure during the charge and discharge processes [9]. Typically, electrodes are composed of three materials, the active material, the conductive additive and the polymer binder. The first one is responsible for storage and release of lithium-ions, the second one enhances the electrical conductivity of the electrode and the last one is responsible for aggregating all components, providing structural integrity and adhesion between composites and to the current collectors [10].

In recent years, additive manufacturing has been associated with the production of battery components. The most used techniques in this field are spray printing, flexography printing, screen printing, inkjet printing or three-dimensional (3D) printing. Supported by the possibility to produce objects layer-by-layer, in the near-final format and significantly reducing the waste of materials, these techniques have been gaining relevance [11]. Rheological properties and morphology are two characteristics that play a key role during the printing process and determine the parameters of the printing system. The most common approach nowadays involves printing individual components and then assembling them into a complete battery device [12].

Direct-Ink Writing (DIW) is a 3D printing technique that is being increasingly used in printed batteries due to their fast prototyping capability, high manufacturing efficiency, scalability, low cost and simplicity [13]. This technique allows to tailor printed layers geometry, porosity and size, while providing precise control over electrode thickness. 3D printing technology achieves layer-by-layer objects using a computer-aided (CAD) design, eliminating the need for specialized molds or masks for individual parts [14].

Several active materials have been developed to be used as active materials in cathodes for battery applications, mainly based on cobalt, iron, manganese and nickel ($LiCoO_2$, $LiFePO_4$, $LiMn_2O_4$, $LiNiO_2$ and others) [15] elements, that have been implemented with different additive manufacturing techniques. In particular, several works have been developed in the last years for LFP based cathode development [16–19], addressing sustainability (absence of cobalt), thermal stability and electrochemical properties of the material and the processing by Direct-Ink Writing (DIW) and Inkjet printing (IJP). Different strategies have been implemented, varying the active material solid content [16], controlling the electrode microstructure and flexibility [17] and improving cathode thickness [18]. Research focusing on the use of DIW printing for battery component production has been performed with different active material solid contents. It was concluded that the presence of optimal porosity, pore size and distribution, controlled through DIW printing technique, improve rate capability of the batteries, reaching 82 mAh g^{-1} at 10C-rate, for the samples produced with lower temperature direct writing technique and a solid content of 0.467 g mL^{-1} [16]. Concerning the focus on the capability to control porosity and thickness of the electrodes, it was assessed that DIW printing technology allows to enhance active material loading, energy density and cycling stability, reaching a discharge capacity value of 121.7 mAh g^{-1} at 0.5C-rate, after 200 cycles and an energy density of 350 Wh.kg^{-1}, for the LFP battery containing 15.9 mg cm^{-2} of active material loading. Regarding LCO active material, Xu et al., [20], studied the production and electrochemical performance of LCO thick cathodes with ordered array structures, using DIW printing techniques. The research shows the benefits of using DIW for the development of the array structures, reducing the electrode tortuosity and concentration polarization and improving ionic transport pathways. These improvements influence positively the electrochemical stability of batteries, driving to a capacity retention, at 2C-rate, up to 82%. Considering LMO active material, Airoldi et al. [21] applied a similar approach, using DIW to develop 3D-patterned thick cathodes with high solid loading, very low solvent amounts, and fast processing, by reducing and simplifying also the drying process and the overall fabrication method. The printing technique also allows to improve the specific and areal capacity, reaching values of 113 mAh g^{-1} and 2.3 mAh cm^{-2}, at 0.1C-rate, respectively. These improved properties are supported by the enhanced diffusion coefficient, with a value of $1.85x10^{-13}$ cm^2 s^{-1} and lower charge transference resistance of 94 Ω cm^{-2}.

To better understand the influence of the manufacturing techniques on the cathode's properties, in this work, cathodes based on the most commonly used active materials (Lithium Iron Phosphate ($LiFePO_4$, LFP), Lithium Manganese Oxide ($LiMn_2O_4$, LMO) and Lithium Cobalt Oxide ($LiCoO_2$, LCO) were produced using conventional Doctor Blade (DB) and DIW and tested in lithium-ion batteries. The direct comparison between both manufacturing techniques, maintaining the same experimental conditions (temperature, slurry preparation and dimensional architecture) and materials will allow to better understand the technique impact on cathodes properties. Cathodes were produced and characterized in terms of morphology and chemical structure, allowing to evaluate the effect of the manufacturing process on cathode electrochemical characteristics and battery performance.

2. Experimental section

2.1. Cathode preparation

The cathode slurries were produced according to previous works [22]. The active materials were obtained from Phostech Lithium, in the case of LFP, and NEI corporation - Nanomyte in the case of LMO and LCO. The conductive additive, carbon black (C45, Super P) was obtained from Timcal Graphite & Carbon, Switzerland, and the polymer binder, poly(vinylidene fluoride) (P(VDF), from Solvay. These materials were used in a weight ratio (%) of 80:10:10, respectively. The solvent, N-methyl-2-pyrrolidone (NMP), was obtained from Fluka and was used

in a solvent/polymer weight ratio of 97:3, for improved polymer dissolution and particle dispersion.

In Fig. 1 the production process is schematically represented. It starts with the polymer binder dissolution and then, the conductive additive and active material were added. The solution was placed under magnetic stirring for 1 h 30 min, dispersed in ultrasonic bath for 1 h and, finally, magnetically stirred again for 30 min. After that, the obtained slurry was filled into a 10 mL plastic syringe attached to a 0.5 mm diameter needle (viscosities around 2 Pa s^{-1} at a shear rate of 160 s^{-1}). The printing procedure was carried out using a Single Head 3D Bioprinter, printing on an aluminium substrate with the printing parameters adjusted taking into account the materials used. The printing speed was 20 mm s^{-1} and a needle tip-to-substrate distance of 0.5 mm. A square of dimensions 4 × 4 cm was obtained after solvent evaporation, later cut into circles with a diameter of 8 mm. The obtained squares were placed in an oven (P-Selecta) at 60 °C for 2 h until complete solvent evaporation.

Three different active materials (LFP, LMO and LCO) samples were manufactured by two different printing techniques (Doctor Blade - DB or Direct-Ink Writing - DIW) and, in the following, will be identified as LFP DB, LFP DIW, LMO DB, LMO DIW, LCO DB and LCO DIW, considering the active material and the printing technique.

2.2. Characterization techniques

2.2.1. Morphological and physical-chemical evaluation

The surface and cross-section morphology of the prepared cathodes was characterized by Scanning Electron Microscopy (SEM, NanoSEM-FEI Nova 200 equipment, with an accelerating voltage of 10 kV and a magnification of 2500x). Energy Dispersive X-ray Spectroscopy (EDS, Pegasus X4M (EDS/EBSD)) was used to evaluate chemical elements from the different active materials. Before the measurements, the samples were coated with a thin gold layer (Polaron, E 6700 model). Using a homemade "bend tester", based on metal rods with diameters between 10.0 and 1.5 mm, the flexibility and adhesion of the prepared cathodes with the current collector was tested.

2.2.2. Modulated Photothermal Radiometry-Infrared

Modulated Photothermal Radiometry-Infrared (PTR) is a frequency-domain technique that uses intensity-modulated excitation to generate *thermal waves* in a sample. By measuring the amplitude and the phase lag of the resulting infrared emission, the material's thermal properties can be determined, namely the thermal diffusion time and the thermal diffusivity through the sample's thickness. By changing the modulation frequency, one can control the penetration depth and the thermal regime (thickness) of the sample. When the thermal diffusion length is approximately equal to the thickness, the phase shift of the radiometric signal exhibits its maximum sensitivity to the material's internal boundaries. Due to this, the technique is widely used to analyze thin films and coatings deposited on appropriate substrates. A detailed description of the technique and its application to thin films and coatings can be found in Refs. [23,24].

A 532 nm DPSS laser, modulated by an acousto-optic modulator, induces periodic temperature oscillations (thermal waves) on the sample surface. The modulation frequency ranges from near-DC up to 200 kHz, enabling depth-resolved measurements spanning from the millimeter scale down to thin films of less than 1 μm. The infrared (IR) emission from the sample surface is collected and focused onto a nitrogen-cooled MCT detector (Judson-Infrared JD15-D12, spectral range 2–12 μm) using BaF2 optics and an IR filter, which also shields the detector from stray light. A two-phase lock-in amplifier (SR865A) extracts the periodic IR signal at the excitation frequency, effectively isolating the thermal response from the larger DC radiation background. The resulting in-phase and out-of-phase components are used to determine the thermal wave amplitude and its phase lag relative to the excitation. The entire measurement process is automated, with data recorded as a function of the modulation frequency. Since in modulated photothermal radiometry the thermal diffusion length varies with the modulation frequency of the incident radiation, the extremum (maximum or minimum) of the phase curve as a function of frequency provides information regarding the thermal diffusion time and the thermal effusivity ratio (sample/substrate). In the present study, the maxima are observed within a specific region of interest located between 120 and 200 Hz.

2.2.3. Battery assembly and electrochemical characterization

For battery analysis, Swagelok-type half-cells were assembled in a homemade argon-filled glovebox (H_2O, O_2 < 1 ppm). The half-cells consisted in a working cathode (8 mm of diameter) relying on the prepared samples, glass microfiber filters (Whatman), as the separator, embedded in an electrolyte solution (Sigma-Aldrich, 1 M lithium hexafluorophosphate ($LiPF_6$) in a mixture of EC:DEC (1:1 v/v)) and a 9 mm metallic lithium disk as reference electrode.

All the assembled half-cells were submitted to electrochemical impedance spectroscopy (EIS) tests, before and after cycling using an Autolab PGSTAT 12 station in the frequency range from 1 to 10 mHz and with an amplitude of 10 mV. Galvanostatic cyclic tests were performed with a Landt CT2001A instrument, using a voltage range between 2.5 and 4.2 V (LFP), 3.0–4.3 V (LMO) and 3.0–4.35 V (LCO), at room temperature, and with different current densities (C/8-, C/5-, C/2-, 1C- and 2C-rate, where C = 170, 148 and 274 mA g^{-1} for LFP, LMO and LCO

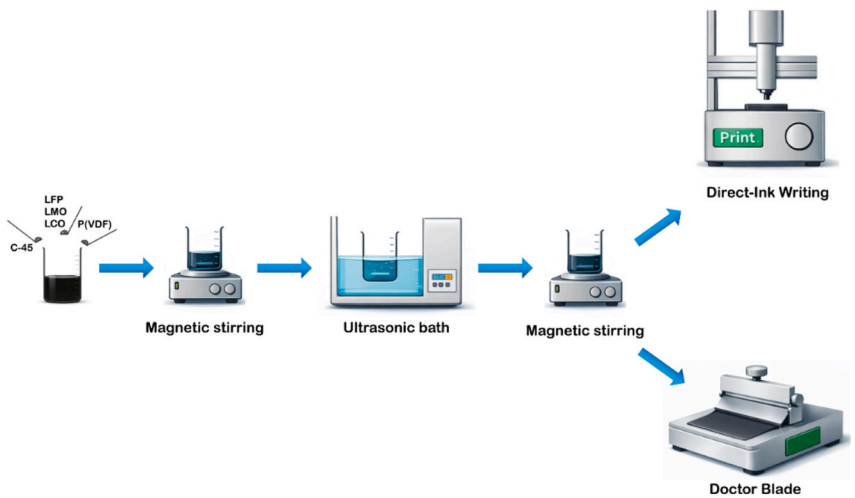


Fig. 1. – Schematic representation of the cathodes' preparation by direct-ink writing (DIW) and doctor blade (DB) techniques.

active materials, respectively. The electrodes prepared both by DB and DIW techniques have 8 mm diameter with active areal mass loading around 4.5 – 5 mg cm^2, after a calendaring process (150 N mm^{-1}). The cells were evaluated considering their rate performance and cycle stability for 50 cycles with the different C-rates (10 cycles each) and 200 cycles at C- and 2C-rates, respectively.

The electrochemical window of the cathodes was evaluated by cyclic voltammetry (CV) at different scan rates (0.0001, 0.0002, 0.0003, 0.0004 and 0.0005 V s^{-1}) in a potential range between 2.5 and 4.2 V for LFP and 2.5–4.6 V for LMO and LCO active materials. Through the different scan rates, the apparent lithium-ion diffusion was calculated based on the Randles-Sevcik equation (Equation (1)) [25]:

$$I_P = 2.69 \times 10^5 n^{3/2} A C_{Li} v^{1/2} \quad \text{(Eq. 1)}$$

where the peak current (I_P) is related to the apparent diffusion of lithium ions (D_{app}), n is the number of electrons involved in the redox reaction, A is the electrode area, C_{Li} is the lithium concentration and v is the scan rate.

Further, Equation (2) was used to determine the percentage of capacity retention, comparing the theoretical with the experimental discharge capacity:

$$\%\ retention = \frac{Experimental\ capacity}{Theorethical\ capacity} \times 100 \quad \text{(Eq. 2)}$$

where the *experimental capacity* was obtained from the galvanostatic cyclic results and the *theoretical capacity* used from the different active materials were 170, 148 and 274 mAh g^{-1} (indicated by the manufacturer) for LFP, LMO and LCO, respectively.

The overall internal resistance of the cells was evaluated by EIS (PalmSens4) using Nyquist plots in the frequency range of 1000 kHz to 20 mHz.

3. Results and discussion

3.1. Morphological and chemical characterization

The morphology of the prepared cathodes was evaluated by scanning electron microscopy (SEM) to better understand the influence of the different active material particles on the cathode surface and cross-sectional morphology. SEM images of the cathodes containing different active material particles (LFP, LCO, and LMO), prepared by both DIW and DB techniques, are shown in Fig. 2.

Fig. 2 shows a homogenously dispersion and distribution of the different cathode components (polymer binder, active material and conductive additive) for all samples, independently of the active materials and processing technique. Furthermore, all cathodes show the characteristic microporosity associated with the solvent evaporation process during their manufacturing. No significant crack formation and delamination was verified at the cathodes, regardless the different rods

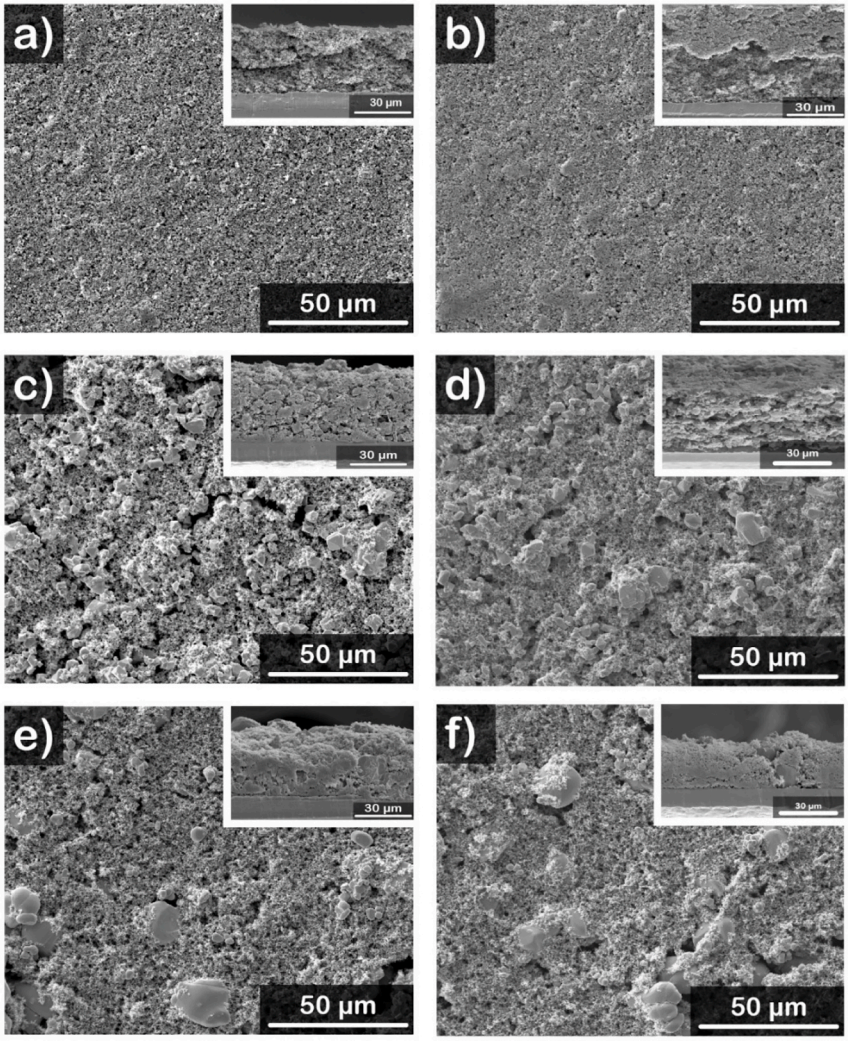


Fig. 2. – Surface and cross-section (inset) images from a) LFP DB, b) LFP DIW, c) LMO DB, d) LMO DIW, e) LCO DB and f) LCO DIW.

diameters (between 10.0 and 1.5 mm) of the bend test, also demonstrating their good flexibility. Also, the rheological properties of the samples are suitable for both manufacturing technique verified at previous works, with viscosities around 2 Pa s^{-1} at shear rate of 160 s^{-1} [26].

Comparing both manufacturing techniques (DIW and DB) it is observed that there is a lower presence of defects on the surface of the samples prepared by DIW. Once the evaporation step in the manufacturing processes is the same for both DIW and DB techniques, the smooth surfaces for the samples prepared by DIW have origin from the capability of the DIW technique to increases the 3D-structural interconnectivity of cathode components [27]. Comparing all the active material cathode samples it is noticeable from surface and cross-sectional SEM images the different size of active material particles LCO (13-14 μm) (Fig. 2e and f) and LMO (11 μm) (Fig. 2c and d) compared to LFP (0.5 μm) (Fig. 2a and b). Cross-sectional SEM images show also less presence of micro cracks at the DIW cathodes compared to DB cathodes, as visualized at surface SEM images. Through the SEM images, the thickness of the cathodes is 39.3 μm (LFP DB), 65.23 μm (LFP DIW), 46.78 μm (LMO DB), 56.88 μm (LMO DIW), 34.73 μm (LCO DB) and 21.23 μm (LCO DIW). The obtained variation of thickness is related to the different active material particles' size and solvent evaporation process, due to different interactions between cathode components and solvent [28]. Furthermore, it was proven [29] that increased cathode thickness not only increases their capacity but also reduce their total cost once vol/wt fractions from components as separators and current collectors is reduced. Sample's porosity was evaluated by the measurements of materials' densities and volume fraction [30]. The porosity percentages of 56 ± 2 % (LFP DB), 54 ± 2% (LFP DIW), 56 ± 2 % (LMO DB), 58 ± 2 % (LMO DIW), 52 ± 2 % (LCO DB) and 60 ± 2 % (LCO DIW) were obtained for the different samples. Though the values are close to each other, DIW technique leads to an increase in porosity for LCO and LMO active materials and a decrease for LFP, when compared to DB prepared samples. The porosity results are related to the different active materials sizes, where small particles led to higher packing densities decreasing the cathode's porosity [31].

The chemical elements from the different active materials were analysed by EDS (Fig. S1) technique and the weight percentage of each element was assessed and shown at Table 1.

The observed chemical elements from the active materials (LFP, LCO and LMO) studied correspond to their specific chemical composition and stoichiometry, without the presence of any impurity. The carbon element observed at all the active materials is related to the presence of the conductive additive (C45) in the overall cathode composition, allowing suitable electronic transport of electron during the charge and discharge processes [32].

3.2. Battery electrochemical characterization

The cyclic voltammetry (CV) of the different cathodes was analysed to verify the redox reactions from each active material, their electrochemical kinetics and to evaluate the influence of the production technique in the cathode redox response. The room temperature CV results at different scan rates and the voltage value for each redox peak are shown in Fig. 3a–f and Table 2, respectively, for all samples. To better understand lithium-ion mobility within the different cathodes, the apparent diffusion coefficient was calculated by the Randles-Sevcik equation (Eq. (1)), Table 2).

Table 1
– Chemical elements from the different active materials of the cathodes.

Samples	Elements/Atomic %					
	C	O	P	Fe	Co	Mn
LFP DIW	20.96	48.20	14.25	16.59	–	–
LCO DIW	10.31	57.75	–	–	31.94	–
LMO DIW	52.94	32.13	–	–	–	14.93

Both cyclic voltammograms from LFP samples (Fig. 3a and b) present electrochemical reversibility for lithium-ion. The characteristic redox behaviour of this active material is indicated by the two symmetrical peaks observed between around 2.8 - 4.0 V and 2.6 - 4.2 V for DB and DIW LFP cathode samples, respectively (Table 2). The mentioned values correspond to reduction - oxidation voltages at the peak related to the deintercalation - intercalation processes (Fe^{3+}/Fe^{2+}) of the lithium-ion within the LFP electrode, respectively [33]. Comparing CV results from LFP DB and LFP DIW it is verified that the separation between redox peaks (Table 2) are lower for sample LFP DB (1.2 V compared to 1.6 from LFP DIW, at the same scan rate of 0.0005 V s^{-1}) demonstrating a higher polarization to the LFP DIW. However, the LFP DIW shows thinner redox peaks indicating higher performance through the higher lithium-ion diffusion [34]. This behaviour can be also associated to the slight decrease of LFP DIW porosity percentage compared to LFP DB and the higher thickness for LFP DIW, allowing higher electrolyte uptake within the electrode. To study the lithium-ion diffusion, the apparent diffusion coefficient of both samples was calculated, showing a higher diffusion for the LFP DIW (3.70×10^{-7} cm^2 s^{-1}) cathode compared to the LFP DB (1.71×10^{-7} cm^2 s^{-1}) one, associated to the increase in peaks intensity and confirming the improved performance of the LFP DIW cathode (Table 2).

Considering the cyclic voltammetry results for LMO based cathodes (Fig. 3c and d), the characteristic redox behaviour of this active material is observed with high reversibility during the oxidation and reduction processes for both used manufacturing techniques (Table 2). A redox reaction with two steps between 3.5 V and 4.5 V (vs. Li^+/Li) is observed originated from the transition Mn^{3+} and Mn^{4+}. Furthermore, a redox reaction is observed between 2.0 V and 3.5 V derived from the formation of tetragonal $Li_2Mn_2O_4$ due to the full transition of $Mn^{3+/4+}$ to Mn^{3+} [35]. This last redox reaction shows that the presence of $Li_2Mn_2O_4$ decreases the kinetics of the lithium-ion insertion, reducing battery performance [36]. Considering this effect, the cutoff voltages used for battery performance evaluation were 3.0 V and 4.3 V for discharge and charge, respectively. Comparing the results for the cathodes prepared by the two manufacturing techniques, it is observed a slight decrease in the distance between the redox peaks for the samples prepared by DIW compared to DB (from 0.4 to 0.3 V at first step and 0.2 to 0.1 V at second step), demonstrating a good connectivity between all cathode components and their suitable distribution within a 3D network, also contributing to the increase of electrolyte uptake capability due to high porosity and higher thickness [37]. Furthermore, a superior apparent diffusion coefficient of the LMO DIW (6.73×10^{-7} cm^2 s^{-1}) is observed compared to LMO DB (4.16×10^{-7} cm^2 s^{-1}).

Considering both LCO cathodes, cyclic voltammetry (Fig. 3e and f) shows the characteristics reversible redox peaks of the LCO active material between around 3.8 and 4.5 V. The obtained peak voltages from LCO DB and LCO DIW correspond to the phase transition among two O3 phases during charge and discharge process [38]. Comparing CV results for LCO DB and LCO DIW, a slight decrease in the distance between both redox peaks for LCO DIW (0.6 V) is observed, indicating that DIW printing decreases the polarization of the cathode also supported by the higher capability of electrode uptake by the electrolyte due to its increased porosity [39]. However, a slight increase of apparent diffusion coefficient (7.42×10^{-7} cm^2 s^{-1}) indicates that the cathode developed by DB technique show improved lithium-ion diffusion compared to the one developed by DIW.

The room temperature fifth cycle of the charge and discharge profiles from the different cathodes manufactured by DB and DIW at the C/8-, C/2- and 2C-rates are presented in Fig. 4a–c. The characteristic voltage plateau of the LFP active material intercalation/deintercalation between the 3.2 and 3.6 V is observed in Fig. 4a. This behaviour is revealed due to the transition from the $LiFePO_4$ and $FePO_4$ structures. Also, the observed oblique line at higher specific capacities demonstrates the capacitive storing behaviour of the structure [40]. The characteristic polarization

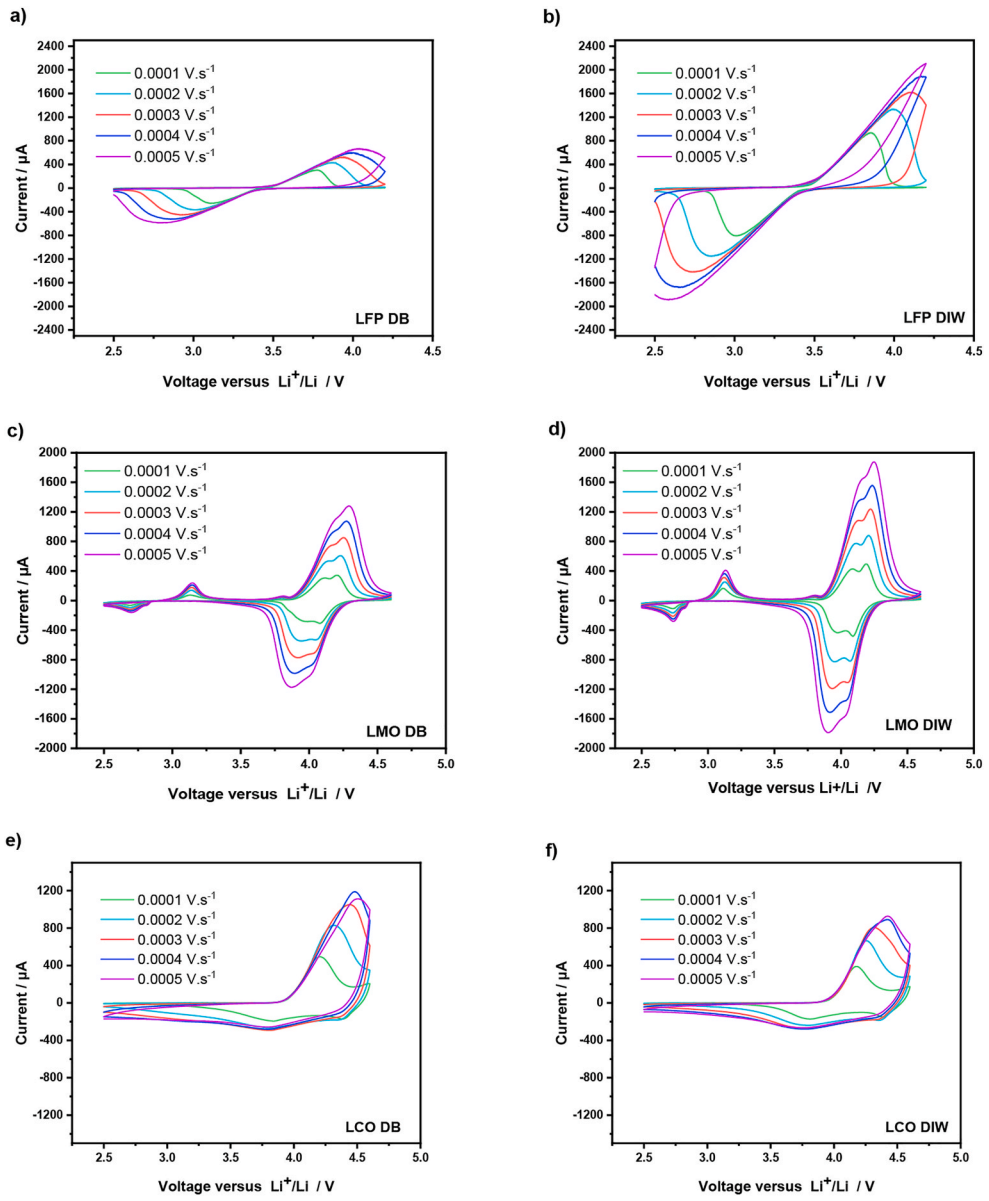


Fig. 3. – Cyclic voltammetry versus Li^+/Li at different scan rates of: a) LFP DB, b) LFP DIW, c) LMO DB, d) LMO DIW, e) LCO DB and f) LCO DIW printed cathodes.

Table 2
– Electrochemical properties obtained from the cyclic voltammetry measurement at 0.0005 V s^{-1} and the respective apparent diffusion coefficient (D_{app}, Eq. (1)) of lithium ions for the different samples.

Samples	$E_{p\ Oxi.}$/V	$E_{p\ Red.}$/V	Peaks separation/V	$D_{app}/\times 10^{-7}$ cm^2 s^{-1}
LFP DB	4.0	2.8	1.2	1.71
LFP DIW	4.2	2.6	1.6	3.70
LMO DB	4.3/4.2	3.9/4.0	0.4/0.2	4.16
LMO DIW	4.2/4.1	3.9/4.0	0.3/0.1	6.73
LCO DB	4.5	3.8	0.7	7.42
LCO DIW	4.4	3.8	0.6	7.30

effect is observed with the increase of C-rate [41], resulting in an increase of the distance between the plateaus and the dropping of the specific capacity. Comparing both manufacturing techniques, it is verified that LFP DIW cathodes shows higher specific capacity at all C-rates (discharge capacity of 137.5, 130.2 and 84.0 mAh g^{-1} at C/8-, C/5- and 2C-rate) compared to LFP DB ones (discharge capacity of 134.8, 123.7 and 82.0 mAh g^{-1} at C/8-, C/5- and 2C-rate). For the LMO active material, Fig. 4b presents the characteristic voltage plateau between the 3.8 and 4.2 V due to the intercalation/deintercalation of lithium-ion, originating the transition between Mn^{3+} and Mn^{4+} [42]. In the LMO cathode, the manufacturing technique DB (discharge capacity of 100.1, 95.8 and 83.8 mAh g^{-1} at C/8-, C/5- and 2C-rate) and DIW technique (discharge capacity of 99.2, 94.6 and 78.7 mAh g^{-1} at C/8-, C/5- and 2C-rate) prepared cathodes show similar responses, as the maximum LMO experimental specific capacity is reached (100 mAh g^{-1}) for both samples (Fig. 4b). Fig. 4c shows the characteristic voltage plateau of the LCO active material around 3.8 and 4.4 V attributed to the intercalation/deintercalation of lithium-ion within the LCO structure [38]. In general, the LCO DIW cathode shows similar specific capacity (discharge capacity of 145.7, 132.0 and 111.3 mAh g^{-1} at C/8-, C/5- and 2C-rate) compared to LCO DB (discharge capacity of 149.1, 132.3 and 93.0 mAh g^{-1} at C/8-, C/5- and 2C-rate). However, at high C-rate (2C-rate) the LCO DIW shows improved capacity. Once the apparent diffusion of both samples is very similar (Table 2), the presence of cracks in LCO BD surface and the lower distance between peaks of LCO DIW can be associated with the observed behaviour at higher C-rate. To better understand the effect of the manufacturing technique on the different

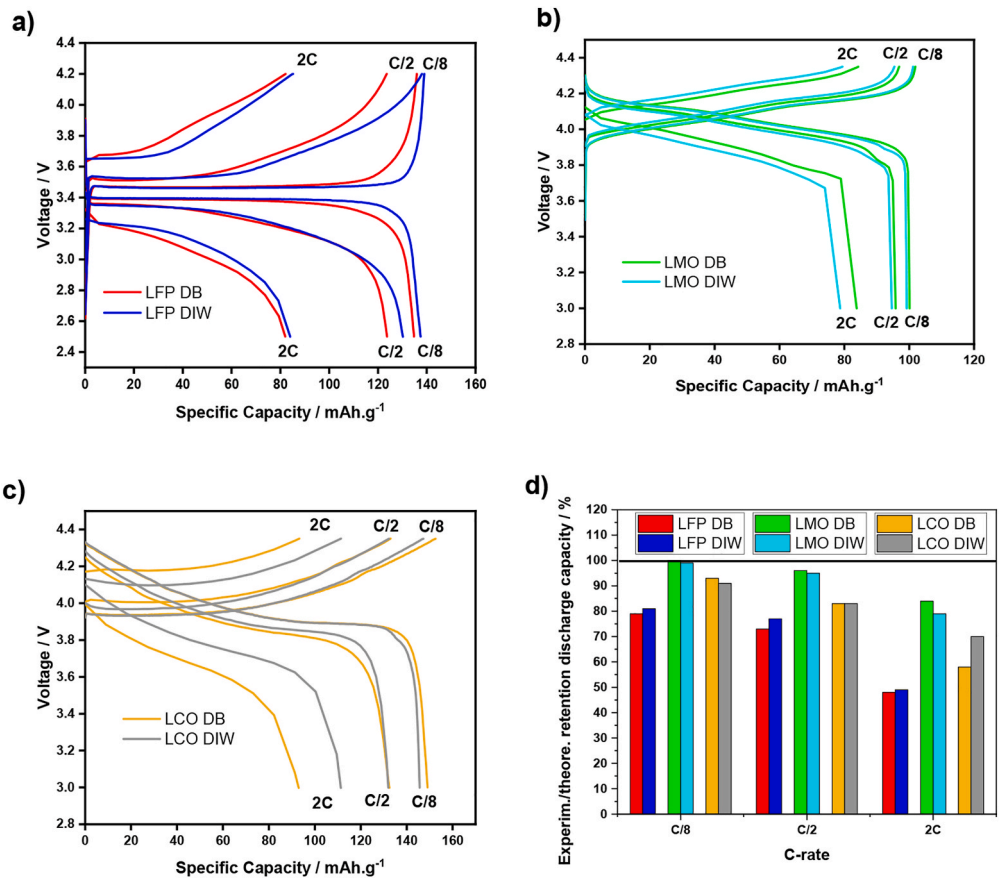


Fig. 4. – Room temperature fifth charge and discharge cycle profiles for a) LFP, b) LMO and c) LCO cathodes at C/8, C/2 and 2C-rates. d) Percentage of capacity retention compared to the theoretical discharge capacities for the different cathodes at C/8, C/2 and 2C-rates.

active material specific capacity at different C-rates, Fig. 4d shows the percentage of capacity retention compared to the theoretical discharge capacities (Eq. (2)) for each C-rate (C/8-, C/2- and 2C-rate) and prepared cathode. From the different cathode active materials, the characteristic intercalation/deintercalation behaviour is observed, independently of the manufacture technique, showing that the use of both techniques does not influence the electrochemical mechanism. However, each manufacturing technique impacts in the specific capacity of the different cathodes with the same active material as can be visualized by the observed different capacity retention in comparison with the theoretical ones. Overall, samples prepared by DIW show improved or at least very similar discharge capacities compared to samples manufactured by DB technique. This behaviour is indicated by the low distance between redox peaks and high apparent diffusion coefficient, related to the absence of cracks in the cathode's structure (Fig. 2 and Table 2).

The room temperature rate performance of the different cathodes at the different C-rates (C/8-, C/5-, C/2-, C- and 2C-rate) are shown in Fig. 5a. All cathodes show a decrease in the discharge capacity with increasing C-rate due to the polarization effect previously mentioned (Table 3) [43]. Comparing all cathodes, the active material that presents lower polarization effect is the LMO cathode with similar discharge capacity for the samples prepared by DB and DIW. Contrary, the LFP cathodes present the highest polarization effect with similar discharge capacity for both manufacturing techniques. On the other hand, the LCO cathodes present similar decreasing polarization effect compared to LFP cathodes, however, at increase C-rates the manufacturing technique DIW influences this behaviour decreasing this polarization effect (increasing the discharge capacity), compared to LCO DB cathode.

Generally, all cathodes show high recovery discharge capacity value at C/8r, with almost the same value at the initial C/8-rate, indicating their high reversibility. Fig. 5b shows the discharge capacity retention (normalized to the C/8) of all cathodes as a function of C-rate. Comparing the active material, it is observed a higher decrease of discharge retention for LFP cathodes at higher C-rate (2C-rate). Comparing both manufacturing techniques for the same active material, almost all active materials demonstrate the same trend of decreasing, however, LCO DB shows a higher decrease in the discharge retention reaching 62%, compared to 76% for LCO DIW.

The stability of the half-cell batteries with the different cathodes was evaluated by charging and discharging the batteries for 200 cycles at C- and 2C-rate (Fig. 5c). Considering the results from Fig. 5c, all batteries show stable response, verified by the high coulombic efficiency between 96% and 99%. Furthermore, the observed decrease in the discharge capacity during the cycles is attributed to the loss of efficiency promoted by material degradation (aging and chemical reactions) during the charge and discharge processes [44]. The capacity retention percentage values obtained from the 100 cycles was 83.38% (LFP DB), 91.04% (LFP DIW), 99.78% (LMO DB), 101.68% (LMO DIW), 68.95% (LCO DB), 90.95% (LCO DIW) at C-rate and 91.72% (LFP DB), 85.39% (LFP DIW), 99.77% (LMO DB), 98.14% (LMO DIW), 77.20% (LCO DB), 88.11% (LCO DIW) at 2C-rate. Comparing both manufacturing techniques for the cathodes with the same active material, it is verified that LMO cathodes present a very similar stability independently the used manufacturing technique. The LFP-based cathodes show a slight superior stability for DIW manufacturing technique, more pronounced at C-rate. However, the LCO DIW shows superior stability compared to LCO DB. At C-rate, LCO DB decreases its discharge capacity around 31% compared to LCO DIW that decreases only 9%. Considering the stability characteristics of both manufacturing techniques for the different active

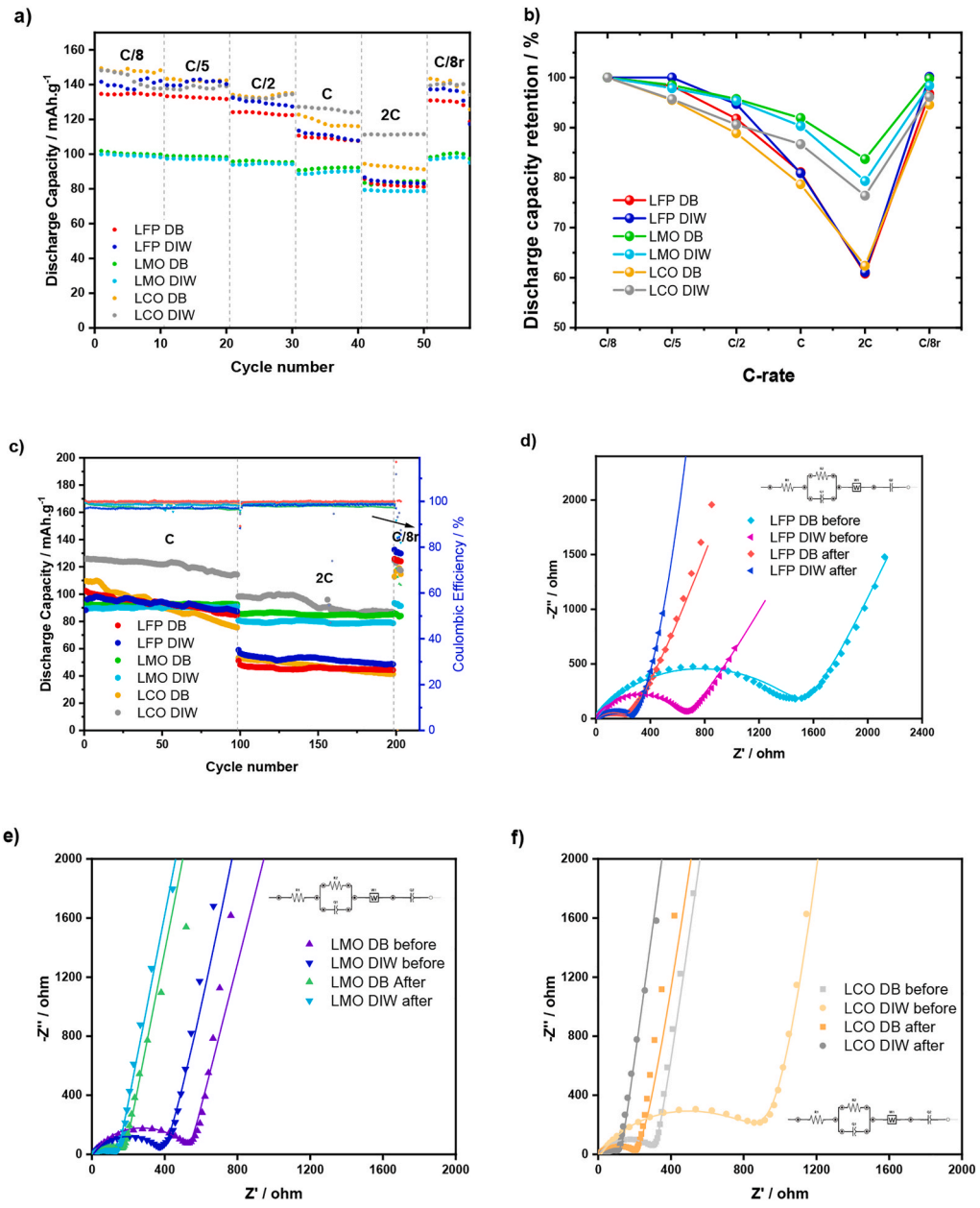


Fig. 5. – a) Discharge capacity as a function of C-rates C/8 and 2C. b) Capacity retention from the discharge process at different C-rates. c) Cycle life stability at C- and 2C-rates as a function of cycle number. Nyquist plots for the different active material cathodes: d) LFP, e) LMO and f) LCO, before and after cycling with the corresponding equivalent circuit and manufacturing technique.

Table 3
– Discharge capacity values for the prepared cathodes at different C-rates from C/8 to 2C and a final rate at C/8 (C/8r) to study the recovery behaviour.

Samples	Discharge capacity at different C-rate/mAh g^{-1}					
	C/8	C/5	C/2	C	2C	C/8r
LFP DB	134.8	132.6	123.7	109.3	82.0	130.4
LFP DIW	137.5	142.7	130.2	111.2	84.0	137.7
LMO DB	100.1	98.6	95.8	92.0	83.8	99.9
LMO DIW	99.2	97.1	94.6	89.6	78.7	97.6
LCO DB	149.1	142.4	132.5	117.3	93.0	141.0
LCO DIW	145.7	139.4	132.0	126.3	111.3	140.1

materials, the DIW printing technique demonstrates to be very suitable for the development of cathodes due to their capacity to equalize or even slightly increase the stability when compared to the established DB technique.

The evaluation of the internal impedance from the different batteries was performed to better understand how the cycling processes affect the cathode. EIS measurements were evaluated at room temperature in the batteries before and after cycling by the analysis of the Nyquist plots (Fig. 5d–f). The Nyquist plots and equivalent circuits for the samples processed by both manufacturing techniques are found in Fig. 5d–. e and f, respectively. The Nyquist plots show two overlapped characteristics semicircles located at high and medium frequencies. Furthermore, at lower frequencies it is identified a straight line. Considering the equivalent circuits, the R1 component represents the resistance of the system (wire, electrolyte). The first and second semicircles correspond to the solid electrolyte interphase and charge transfer resistance (R_{CT}) of the electrodes (R2). The high- and low-frequency capacitances are described by a constant phase element (CPE) CPE1. The obtained value for each fitted component is summarized in Table S1 provided as supplementary

material. Finally, the lithium-ion diffusion is characterized by a straight line at low-frequencies represented by the Warburg impedance (W) [45, 46]. Considering the obtained results, it is observed a decrease of the overall resistance (obtained from R2) for all cathodes, independently the manufacturing technique and the active material, when compared the measurements before and after cycling (Table 4).

This behaviour is explained by the adjustment of the internal cathode' components allowing an increased electrolyte penetration and the formation of a stable SEI. LFP and LCO show higher overall resistance before cycling. Considering the apparent Li-ion diffusion results from LFP and LCO for both BD and DIW process, it was verified that for LFP active material the manufacturing process shows higher influence, leading to higher diffusion values when DIW technique is used. On the other hand, when LCO is used, the cathode maintains almost the same diffusion value. Comparing diffusion results with the EIS results for both LCO and LFP and considering the results from rate performance (Fig. 5a) it is demonstrated that LCO cathodes need more cycles to stabilize their SEI and consequently their discharge capacity value, first verified from the first cycles from rate performance results and for the high overall resistance before cycling [47]. Comparing the manufacturing techniques for the same active material it is evidenced that after cycling, the DIW cathodes show lower overall resistance, proving improved lithium-ion diffusion and more stable SEI formation.

Considering the obtained discharge capacity values for each DIW sample, the electrochemical comparison with literature is presented in Table 5.

Higher active material percentages do not necessarily guarantee superior performance, as seen in earlier reports where even 80–95% active material yielded relatively low specific capacities and limited cycle life. In contrast, lower active material content (e.g., 40%) sometimes delivered higher capacities and moderate cycling stability, suggesting that electrode formulation and conductivity play a critical role alongside composition (e.g., use of carbon nanofibers). Notably, the results from this work show a balanced and improved performance across all three chemistries at 80% active material. Both LFP and LCO electrodes achieved higher specific capacities (137.5 and 145.7 mAh g^{-1}, respectively) with significantly enhanced cycling stability (200 cycles), outperforming most benchmarked studies. Although LMO exhibited a comparatively lower capacity (99.2 mAh g^{-1}), it still demonstrated excellent cycle life, demonstrating improved electrode durability. Overall, these findings highlight that optimizing electrode design and processing strategy, rather than simply maximizing active material content, is key to achieving high capacity and long-term stability.

Security and safety are essential in lithium-ion batteries, as failure events that can escalate to thermal runaway leading to explosion, fire and release of toxic gases. Thermal properties such as thermal diffusivity are important to evaluate the cathodes safety and stability during charge/discharge processes [50]. Considering the high importance of the thermal properties, the DIW cathodes' thermal diffusivity was estimated, due to their improved electrochemical properties compared to DB cathodes. The samples under study present significant challenges for this technique, since the materials were pressed onto an aluminum foil substrate. Aluminum exhibits complex infrared behavior, characterized by low emissivity and high reflectivity, which can distort the radiometric signals used in the fitting process. Furthermore, the pressing process introduced significant thermal contact resistance at the interface, adding complexity to signal interpretation and quantification. The cathodes porosity also plays a role in the measured signals, once higher porosity systems like the LCO present a lower relative thermal diffusivity.

Despite these challenges, the experimental data follow the expected behavior for a two-layer system. While the absolute numerical results are overestimated, the trends observed in the phase and amplitude curves (Fig. S2) allow for a consistent comparative analysis, assuming a uniform substrate contribution across all measured samples. To extract reliable values for the thermal diffusivity, the "phase dip" induced by the aluminum would require high-precision fitting using a multi-layer heat diffusion model to decouple the sample's intrinsic diffusion time from the substrate's rapid heat dissipation and the interfacial resistance.

The trend of the thermal diffusivity obtained from the different cathodes show that LCO < LFP < LMO. Thus, the higher thermal diffusivity stands for LMO based cathodes (approximately 3 times higher than LCO). The LFP cathode value, about 1.4 times higher than LCO which presents the lower thermal diffusivity. The obtained thermal behaviour correlates with theoretical simulation studies [51] where the LCO and LMO cathodes show similar thermal response, different from the one of LFP (Fig. S2). The observed thermal diffusivity behaviour is related to the intrinsic thermal characteristics of the particles together with the cathodes' porosity [52]. All the samples present suitable thermal behaviour making the DIW technique a suitable technique to tune the cathode's thermal behaviour by controlling porosity [53].

Table 4
– Room temperature overall resistances for the prepared cathodes before and after cycling.

Samples	Overall resistance/Ω	
	Before	After
LFP DB	1572.7	296.8
LFP DIW	672.8	275.3
LMO DB	569.1	205.8
LMO DIW	404.9	172.3
LCO DB	336.5	220.3
LCO DIW	1124.8	142.3

Table 5
– Electrochemical properties of cathodes manufactured by DIW technique with similar preparation conditions and studied active materials.

Active material percentage	Active material	Specific capacity/mAh g^{-1}	Cycling stability/ cycle number	Ref.
80	LFP	82 at 0.1C	30	[16]
40	LFP	156 at 0.2C	100	[48]
95	LCO	102.9 at 0.2C	40	[20]
40	LCO	137 at 0.2C	100	[48]
85	LMO	117 at 0.1C	21	[49]
80	LFP	137.5 at 0.125C	200	This work
80	LCO	145.7 at 0.125C	200	This work
80	LMO	99.2 at 0.125C	200	This work

4. Conclusion

Cathodes with LFP, LMO and LCO active materials were developed by two different manufacturing techniques, doctor blade (DB) and Direct-Ink Writing (DIW), in order to evaluate their influence on cathode's properties and performance when assembled into lithium-ion half-cells. It is shown that cathode components (polymer binder, active material and conductive additive) are homogenously dispersed and distributed without clusters and agglomerations for all cathodes, independently of the processing technique. Manufacturing technique, on the other hand, influences the cathodes morphology, showing smooth surfaces for samples prepared by DIW due to increased 3D-structural interconnectivity of the cathode components.

CV shows that the DIW technique lowers the distance between redox peaks, when compared to DB technique, from 0.1 to 0.2 V for LMO and

0.7 to 0.6 V for LCO, however, for LFP it is verified an increase from 1.2 to 1.6 V. Furthermore, cathodes prepared by DIW present higher apparent lithium-ion diffusion coefficient (LFP DIW 3.70×10^{-7} cm^2 s^{-1} and LMO DIW 6.73×10^{-7} cm^2 s^{-1}), compared to DB cathodes, however, in LCO cathodes is verified almost the same apparent lithium-ion diffusion coefficient when DIW technique is used. The use of DIW technique as cathode manufacturing technique, overall, maintains or even induces higher lithium-ion diffusion, together with good connectivity between all cathode components and good distribution within a 3D network of cathode. The evaluated half-cells demonstrated a correlation with the diffusion, morphology and overall resistance of the cathodes showing discharge capacities at C/8-rate of 134.8, 137.5, 100.1, 99.2, 149.1 and 145.7 mAh g^{-1} for LFP DB, LFP DIW, LMO DB, LMO DIW, LCO DB and LCO DIW, respectively. Both manufacturing techniques, for the same active material, demonstrated the same tendency of decreasing the discharge capacity over C-rates, due to polarization effect, however, at 2C-rate LCO DB shows a higher decrease in the discharge retention reaching to 62%, compared to 76% of LCO DIW. Further, the thermal and electrochemical stability of the half-cells with cathodes prepared by DIW is the same of even slightly better that the ones prepared by the well-established DB technique. DIW processing technique induces improved cathode surface morphology with low cracks formation, lower overall resistances and superior performance with simple scalability for high-fidelity electrode manufacturing, allowing also specific battery designs. Overall, it is demonstrated the suitability of DIW technique to produce cathodes with different active fillers, in order to tailor battery characteristics for specific applications.

CRediT authorship contribution statement

Rafael S. Pinto: Formal analysis, Investigation, Methodology, Validation, Visualization, Writing – original draft, Writing – review & editing. **Francisco Macedo:** Formal analysis, Investigation, Validation, Visualization, Writing – original draft, Writing – review & editing. **Maria M. Silva:** Formal analysis, Investigation, Validation, Visualization, Writing – original draft, Writing – review & editing. **Carlos M. Costa:** Conceptualization, Formal analysis, Funding acquisition, Investigation, Project administration, Supervision, Validation, Visualization, Writing – original draft, Writing – review & editing. **Senentxu Lanceros-Mendez:** Formal analysis, Funding acquisition, Investigation, Project administration, Supervision, Validation, Writing – original draft, Writing – review & editing. **Renato Gonçalves:** Conceptualization, Formal analysis, Funding acquisition, Investigation, Project administration, Supervision, Validation, Visualization, Writing – original draft, Writing – review & editing.

Declaration of competing interest

The authors declare that they have no known competing financial interests or personal relationships that could have appeared to influence the work reported in this paper.

Acknowledgement

The authors thank the Portuguese Foundation for Science and Technology (FCT) for financial support under the framework of Strategic Funding UID/00686/2025: Chemistry Centre of the University of Minho (CQ-UM) (DOI: https://doi.org/10.54499/UID/00686/2025) and UID/04650/2025: Physics Centre of Minho and Porto Universities (CF-UM-UP) (DOI: https://doi.org/10.54499/UID/04650/2025) and under project 10.54499/2022.03931.PTDC funded by national funds through FCT. The authors also thank the FCT for financial support under FCT Grant 2021.07361.BD (RSP). This study forms part of the Advanced Materials program and was supported by MCIN with funding from European Union NextGenerationEU (PRTR-C17.I1) and by the Basque Government under the IKUR program and Elkartek programs.

Appendix A. Supplementary data

Supplementary data to this article can be found online at https://doi.org/10.1016/j.jpowsour.2026.240442.

Data availability

Data will be made available on request.

References

[1] R. Golmohammadzadeh, et al., Current challenges and future opportunities toward recycling of spent lithium-ion batteries, Renew. Sustain. Energy Rev. 159 (2022) 112202.
[2] S. Anwani, R. Methekar, V. Ramadesigan, Resynthesizing of lithium cobalt oxide from spent lithium-ion batteries using an environmentally benign and economically viable recycling process, Hydrometallurgy 197 (2020) 105430.
[3] T. Ingsel, R.K. Gupta, Solid-State rechargeable lithium-ion batteries: component chemistries and battery architectures, in: Solid State Batteries Volume 1: Emerging Materials and Applications, American Chemical Society, 2022, pp. 21–37.
[4] C. Shang, K. Cheng, The present applications and prospects of lithium-ion battery, in: 5th International Conference on Mechatronics and Computer Technology Engineering (MCTE 2022), vol 12500, SPIE, 2022.
[5] Y. Huang, et al., Chelate reconstruction with a H2O-poor and zinc-rich interface toward robust anti-corrosion Ah-level zinc aqueous batteries, Energy Storage Mater. 84 (2026) 104821.
[6] H. Tan, et al., Polydentate ligand stabilizes electrolyte and interface layer for anti-corrosion and selective-deposited Zn metal aqueous batteries, Adv. Funct. Mater. 35 (28) (2025) 2423945.
[7] L. Elbinger, et al., Beyond lithium-ion batteries: recent developments in polymer-based electrolytes for alternative metal-ion-batteries, Energy Storage Mater. 65 (2024) 103063.
[8] W. Zhao, A forum on batteries: from lithium-ion to the next generation, Natl. Sci. Rev. 7 (7) (2020) 1263–1268.
[9] R. Wagner, et al., Current research trends and prospects among the various materials and designs used in lithium-based batteries, J. Appl. Electrochem. 43 (5) (2013) 481–496.
[10] M. Kotal, et al., Cathode materials for rechargeable lithium batteries: recent progress and future prospects, J. Energy Storage 47 (2022) 103534.
[11] D. Mouraliraman, et al., 3D printed lithium-ion batteries: an in-depth examination of the advancements in flexibility and stand-alone capability, J. Energy Storage 81 (2024) 110395.
[12] Z. Lyu, et al., Design and manufacture of 3D-Printed batteries, Joule 5 (1) (2021) 89–114.
[13] J. Yan, et al., Direct-ink writing 3D printed energy storage devices: from material selectivity, design and optimization strategies to diverse applications, Mater. Today 54 (2022) 110–152.
[14] J. Bae, et al., High-performance, printable quasi-solid-state electrolytes toward all 3D direct ink writing of shape-versatile Li-ion batteries, Energy Storage Mater. 57 (2023) 277–288.
[15] J.C. Barbosa, et al., Recent advances on materials for lithium-ion batteries, Energies 14 (11) (2021) 3145.
[16] C. Liu, et al., Comparative study on the electrochemical performance of LiFePO4 cathodes fabricated by low temperature 3D printing, direct ink writing and conventional roller coating process, Ceram. Int. 45 (11) (2019) 14188–14197.
[17] M. Cong, et al., Preparation of lithium iron phosphate battery by 3D printing, Ceram. Int. 50 (9, Part A) (2024) 14749–14756.
[18] P. Bao, et al., 3D printing PEDOT-CMC-based high areal capacity electrodes for Li-ion batteries, Ionics 27 (7) (2021) 2857–2865.
[19] A. Shaju, et al., Novel approaches in 3D printing techniques for the development of high-performance micro-batteries, J. Electron. Mater. 54 (3) (2025) 1531–1552.
[20] S. Xu, et al., Optimization of LiCoO2 thick electrodes with low tortuosity for lithium-ion batteries by 3D printing, J. Mater. Chem. A 13 (14) (2025) 9747–9756.
[21] L. Airoldi, et al., Additive manufacturing of aqueous-processed LiMn2O4 thick electrodes for high-energy-density lithium-ion batteries, Batter. Supercaps 3 (10) (2020) 1040–1050.
[22] A. Gören, et al., Influence of solvent evaporation rate in the preparation of carbon-coated Lithium Iron phosphate cathode films on battery performance 4 (5) (2016) 573–582.
[23] J.L. Nzodoum Fotsing, et al., Extremum method: inverse solution of the two-layer thermal wave problem, J. Appl. Phys. 98 (6) (2005).
[24] J. Gibkes, et al., Analysis of multifunctional oxycarbide and oxynitride thin films by modulated IR radiometry, J. Phys. Appl. Phys. 43 (39) (2010) 395301.
[25] Z.-Y. Mao, Y.-P. Sun, K. Scott, Evaluation of apparent lithium-ion diffusion coefficients in FePO4/LiFePO4 cathode material particles from linear non-equilibrium thermodynamics and principle of electroneutrality, J. Electroanal. Chem. 766 (2016) 107–119.
[26] J.C. Barbosa, et al., Poly(vinylidene fluoride-trifluoroethylene-chlorofluoroethylene): a new binder for conventional and printable lithium-ion batteries, ACS Appl. Energy Mater. 4 (12) (2021) 14129–14140.
[27] T. Huang, et al., Direct ink writing of conductive materials for emerging energy storage systems, Nano Res. 15 (7) (2022) 6091–6111.

[28] M. Müller, et al., Effect of nanostructured and open-porous particle morphology on electrode processing and electrochemical performance of Li-Ion batteries, ACS Appl. Energy Mater. 4 (2) (2021) 1993–2003.
[29] C. Imediegwu, et al., Modelling optimum thickness and architecture for lithium-ion battery cathodes, J. Power Sources 614 (2024) 235005.
[30] T. Marks, et al., A guide to Li-Ion coin-cell electrode making for academic researchers, J. Electrochem. Soc. 158 (1) (2011) A51.
[31] P. Minnmann, et al., Designing cathodes and cathode active materials for solid-state batteries, Adv. Energy Mater. 12 (35) (2022) 2201425.
[32] A.S. Alhammadi, H.J. Yun, D. Choi, Investigation of LiFePO4/MWCNT cathode-based half-cell lithium-ion batteries in subzero temperature environments, Ionics 29 (6) (2023) 2163–2174.
[33] J. Xia, et al., In situ coating on LiFePO4 with ionic liquid as carbon source for high-performance lithium batteries, J. Nanoparticle Res. 20 (7) (2018) 196.
[34] S.J. Rajoba, et al., Electrochemical performance of LiFePO4/GO composite for Li-ion batteries, Ceram. Int. 44 (6) (2018) 6886–6893.
[35] V. Siller, et al., Nanoscaled LiMn2O4 for extended cycling stability in the 3 V Plateau, ACS Appl. Mater. Interfaces 14 (29) (2022) 33438–33446.
[36] L.L. De Taeye, P.M. Vereecken, Detrimental MnPO4F and MnF2 formation on LiMn2O4 in the 3 V region, J. Mater. Chem. A 9 (40) (2021) 23256–23268.
[37] J.P. Mwizerwa, et al., 3D-printed activated carbon cross-linked graphene oxide networks as high areal capacity and energy density electrode for lithium-ion batteries, J. Energy Storage 141 (2026) 119454.
[38] J. Qian, et al., Electrochemical surface passivation of LiCoO2 particles at ultrahigh voltage and its applications in lithium-based batteries, Nat. Commun. 9 (1) (2018) 4918.
[39] M. Ohrelius, G. Lindbergh, R.W. Lindström, Polarization effects and aging characterization of lithium-ion batteries for second life applications, J. Power Sources 655 (2025) 237931.
[40] S.-X. Zhao, et al., Improving rate performance of LiFePO4 cathode materials by hybrid coating of nano-Li3PO4 and carbon, J. Alloys Compd. 566 (2013) 206–211.
[41] J. Hedman, F. Björefors, Fiber optic monitoring of composite Lithium iron phosphate cathodes in pouch cell batteries, ACS Appl. Energy Mater. 5 (1) (2022) 870–881.
[42] E. Shahpouri, M.M. Kalantarian, Origin of electrochemical voltage range and voltage profile of insertion electrodes, Sci. Rep. 14 (1) (2024) 14311.
[43] L. Wang, et al., Identifying cathode and anode polarizations during practical high-rate charging/discharging in different Li-ion pouch batteries, Battery Energy 2 (1) (2023) 20220025.
[44] N. Meddings, et al., Application of electrochemical impedance spectroscopy to commercial Li-ion cells: a review, J. Power Sources 480 (2020) 228742.
[45] L.A. Middlemiss, et al., Characterisation of batteries by electrochemical impedance spectroscopy, Energy Rep. 6 (2020) 232–241.
[46] W. Choi, et al., Modeling and applications of Electrochemical Impedance Spectroscopy (EIS) for lithium-ion batteries, J. Electrochem. Sci. Technol 11 (1) (2020) 1–13.
[47] C. Geisbauer, et al., Comparative study on the calendar aging behavior of six different lithium-ion cell chemistries in terms of parameter variation, Energies 14 (11) (2021) 3358.
[48] R.R. Kohlmeyer, et al., Composite batteries: a simple yet universal approach to 3D printable lithium-ion battery electrodes, J. Mater. Chem. A 4 (43) (2016) 16856–16864.
[49] J. Li, et al., A hybrid three-dimensionally structured electrode for lithium-ion batteries via 3D printing, Mater. Des. 119 (2017) 417–424.
[50] J. Nanda, et al., Thermophysical properties of LiFePO4 cathodes with carbonized pitch coatings and organic binders: experiments and first-principles modeling, J. Power Sources 251 (2014) 8–13.
[51] D. Miranda, et al., Effect of the active material type and battery geometry on the thermal behavior of lithium-ion batteries, Energy 185 (2019) 1250–1262.
[52] J.C. Gandert, et al., Effective thermal conductivity of lithium-ion battery electrodes in dependence on the degree of calendering, Energy Technol. 11 (8) (2023) 2300259.
[53] L. Zeng, et al., Direct ink writing 3D printing for high-performance electrochemical energy storage devices: a minireview, Adv. Sci. 10 (32) (2023) 2303716.